Erciyes University Journal of Institue Of Science and Technology

Research Article
10.65520/erciyesfen.1974950

Imprint:
Volume: 42(3)
Year: 2026
Page: 85-108

Muhammed Salih SARIKAYA[a]
Mert Süleyman DEMİRSOY[b*]
Yusuf HAMİDA EL NASER[c]

[a] Dr., Sakarya Applied Science University, salihsarikaya@subu.edu.tr
[b] Dr., Sakarya Applied Science University, mertdemirsoy@subu.edu.tr
[c] Dr., Sakarya Applied Science University, yusufelnaser@subu.edu.tr

* Corresponding Author

Received: 6/19/2026
Accepted: 9/26/2026

Citation:
Muhammed Salih SARIKAYA, Mert Süleyman DEMİRSOY, Yusuf HAMİDA EL NASER (2026). Robust Local Stabilization of the Moore–Spiegel Chaotic Oscillator via Grey Wolf Optimizer-Based Pole Placement. *Erciyes University Journal of Institue Of Science and Technology*, 42(3), 85-108. https://doi.org/10.65520/erciyesfen.*1974950*

Screened by iThenticate for Authors & Researchers

Except where otherwise noted, content in this article is licensed under a Creative Commons 4.0 International license. Icons by Font Awesome.

Robust Local Stabilization of the Moore–Spiegel Chaotic Oscillator via Grey Wolf Optimizer-Based Pole Placement

Abstract

In this paper, the chaotic nature of the Moore–Spiegel system is first confirmed at $T = 36$ *and* $R = 100$ *through a detailed dynamical analysis, and then an optimization-based state-feedback controller is developed for its local stabilization. To stabilize the system, a single-input state-feedback controller is designed, and the closed-loop pole locations are optimized by the Grey Wolf Optimizer (GWO). The optimization objective is defined as a composite performance index that combines the integral of time-weighted absolute error (ITAE), the integral of squared error (ISE), and additional terms penalizing control energy, overshoot, and settling time. To improve robustness, the optimization is carried out using a minimax formulation over three different initial conditions, while four control-theoretic inequality constraints are incorporated through a penalty-based approach. The results of 30 independent runs show that GWO, PSO, and GA all converge to the same well-damped pole configuration* ($\zeta = 0.707$), *yielding the optimal feedback gain* ($K_{opt} = [18.9901, 100.3393, 8.0550]$). *Compared with a conventional pole-placement design, the proposed approach reduces ISE by* 83.9%, *IAE by* 16.5%, *overshoot by* 79.6%, *and control energy by* 94.8%. *These improvements are obtained at the cost of a longer settling time and a higher ITAE than the baseline design, a deliberate trade-off that follows from the lower-gain, well-damped pole configuration. Moreover, the closed-loop system remains stable under* ($\pm$10%) *parametric uncertainty in (T) and (R), with a maximum ITAE deviation below* 35.1%, *and also preserves stability in the presence of measurement noise up to* 10%. *These findings show that GWO algorithm optimization provides an effective, robust framework for the local stabilization of chaotic systems.*

Keywords: *Moore–Spiegel; chaos control; Grey Wolf Optimizer; robust control*

Moore-Spiegel Kaotik Osilatörünün Sağlam Yerel Stabilizasyonu için Gri Kurt Optimizasyon Algoritması Tabanlı Optimal Kutup Yerleştirme Yöntemi

Öz

Bu makalede, Moore–Spiegel sisteminin $T = 36$ *ve* $R = 100$ *parametrelerinde kaotik yapısı önce ayrıntılı bir dinamik analiz ile doğrulanmış, ardından sistemin yerel kararlılığını sağlamak amacıyla optimizasyon tabanlı bir durum geri beslemeli denetleyici geliştirilmiştir. Sistemi kararlı hale getirmek için tek girişli bir durum geri besleme denetleyicisi tasarlanmış ve kapalı çevrim kutup konumları Gri Kurt Optimizasyonu (Grey Wolf Optimizer, GWO) algoritması ile optimize edilmiştir. Optimizasyon amacı, zamanla ağırlıklandırılmış mutlak hata integrali (ITAE), hata karesinin integrali (ISE) ve ayrıca kontrol enerjisi, aşım ile oturma süresini cezalandıran terimleri birlikte içeren birleşik bir performans ölçütü olarak tanımlanmıştır. Dayanıklılığı artırmak amacıyla optimizasyon, üç*

farklı başlangıç koşulu üzerinde minimaks yaklaşımıyla yürütülmüş; ayrıca dört adet kontrol kuramına dayalı eşitsizlik kısıtı ceza tabanlı bir yöntemle probleme dahil edilmiştir. Otuz bağımsız çalıştırmadan elde edilen sonuçlar, GWO'nun $\zeta = 0.707$ *olacak şekilde iyi sönümlü bir kutup konfigürasyonuna GWO, PSO ve GA ile tutarlı biçimde yakınsandığını ve (*$K_{opt} = [18.9901, 100.3393, 8.0550]$*) optimal geri besleme kazancını verdiğini göstermektedir. Klasik kutup yerleştirme tabanlı tasarımla karşılaştırıldığında, önerilen yaklaşım ISE değerinde* %83.9*, IAE değerinde* %16.5*, aşım miktarında* %79.6 *ve kontrol enerjisinde* %94.8 *oranında azalma sağlamıştır. Bununla birlikte bu iyileşmeler, oturma süresinin ve ITAE değerinin referans tasarıma kıyasla artması pahasına elde edilmiştir; söz konusu ödünleşim, düşük kazançlı ve iyi sönümlü kutup konfigürasyonunun bilinçli bir sonucudur. Ayrıca kapalı çevrim sisteminin, T ve R parametrelerindeki* $\pm 10\%$ *belirsizlik altında, maksimum ITAE sapması* %35.1*'nın altında kalacak şekilde kararlılığını koruduğu ve* %10*'a kadar ölçüm gürültüsü varlığında da kararlı çalışmayı sürdürdüğü görülmüştür. Bu bulgular, GWO algoritması tabanlı optimizasyonun kaotik sistemlerin yerel kararlılığının sağlanmasında etkili ve dayanıklı bir çerçeve sunduğunu göstermektedir.*

Anahtar kelimeler: *Moore-Spiegel; kaos kontrolü; Gri Kurt Optimizasyon algoritması; sağlam kontrol*

1. INTRODUCTION

Deterministic chaos describes the bounded yet aperiodic, long-term-unpredictable behaviour exhibited by nonlinear dynamical systems that possess extreme sensitivity to initial conditions and a positive largest Lyapunov exponent [1,2]. Such chaotic dynamics arise across a broad range of engineering and scientific domains (including power systems, mechanical and electromechanical systems, secure communications, and astrophysical convection) where they are frequently undesirable and must be suppressed, stabilized, or otherwise controlled [1,3]. The Moore–Spiegel oscillator is a classical third-order autonomous chaotic system, originally introduced to model the thermally excited nonlinear oscillations of an electrically conducting fluid element in stellar atmospheres [4,5]. Owing to its compact structure and remarkably rich dynamics (encompassing period-doubling, saddle-node, and homoclinic bifurcations as well as fully developed chaos) it has become a widely used benchmark for studies of nonlinear dynamics, synchronization, chaos control, and secure-communication schemes [5,6].

The characterization of a chaotic system follows a well-established analytical methodology built upon the computation of equilibrium points, the Jacobian matrix and its eigenvalues, the phase-space divergence, the Lyapunov exponent spectrum, the Kaplan–Yorke (Lyapunov) dimension, and bifurcation diagrams [7-10]. A positive largest Lyapunov exponent confirms the sensitive dependence on initial conditions that defines chaos, whereas the coexistence at an equilibrium of eigenvalues with positive and negative real parts (that is, a saddle-type instability) is characteristic of systems that generate strange attractors [8,9]. The Lyapunov spectrum is most commonly estimated using Wolf-type algorithms and is routinely reported together with the Kaplan–Yorke dimension and bifurcation diagrams to map the transitions between periodic and chaotic regimes [7,11].

The stabilization of chaotic systems has motivated a large body of control research, drawing on methods such as the Ott–Grebogi–Yorke approach, delayed feedback control, sliding-mode control, adaptive control, and state-feedback control with eigenvalue assignment (pole placement) [12-14]. Among these, state-feedback pole placement is particularly attractive because it relocates the closed-loop eigenvalues to prescribed stable locations through a constant feedback gain, and it can be applied once the chaotic system is linearized about its unstable equilibrium [12,15,16]. The feasibility of arbitrary eigenvalue assignment is guaranteed by the full-rank condition of the controllability matrix, which is verified prior to controller synthesis [14,15].

Despite its theoretical elegance, classical pole placement (rooted in formulations such as the Bass–Gura and Ackermann formulae and in eigenstructure assignment [17,18]) offers no systematic guidance on where the closed-loop poles should be located. The relationship between pole locations and key transient-performance indicators such as overshoot, settling time, and control effort is not transparent, which renders the choice of pole locations largely a trial-and-error exercise for complex systems [19]. Comparable difficulties affect related techniques such as the linear quadratic regulator,

CC: BY-NC-ND

whose weighting matrices must be tuned through a non-trivial, iterative process [20,21]. Pole placement is nevertheless retained here in preference to the linear quadratic regulator because it fixes the closed-loop eigenvalues, and hence the damping ratio, the natural frequency and the stability margin, directly and explicitly, whereas the regulator determines them only implicitly through the weighting matrices. For a third-order single-input plant this yields a compact, physically interpretable and low-dimensional decision vector (three pole parameters instead of the entries of a weighting matrix), and it allows control-theoretic requirements such as a minimum damping ratio and a minimum stability margin to be imposed directly as constraints on the decision variables.

To overcome these difficulties, metaheuristic optimization has been increasingly employed to recast controller-parameter selection as a well-defined optimization problem [19,20]. Genetic algorithms (GA) and particle swarm optimization (PSO) have been widely applied to pole placement and to the tuning of LQR weighting matrices, systematically replacing manual tuning [20,21]. Among the more recent metaheuristics, the Grey Wolf Optimizer (GWO), introduced by Mirjalili et al. [22], has attracted considerable attention; inspired by the social leadership hierarchy and cooperative hunting of grey wolves, it offers conceptual simplicity, few tuning parameters, derivative-free operation, and competitive convergence behaviour [23,24].

Comparative studies indicate that GWO is frequently able to reach optimal controller parameters in fewer iterations than PSO and to cope well with noisy search landscapes, whereas GA tends to deliver robust global search at a higher computational cost [25-27]. GWO has consequently been adopted across a wide spectrum of control problems, including the optimization of state-feedback and LQR weighting matrices [28-30], the tuning of feedback-linearization gains [31], robust control [32], and sliding-mode control design [33,34]; it has also been used for state-feedback stabilization of unstable nonlinear benchmarks such as the inverted and Furuta pendulums, where a stabilizing gain vector of the form $u = -Kx$ is learned directly by the optimizer [35]. Within the chaos domain specifically, metaheuristics (including GWO) have been applied to chaotic-system parameter estimation and control, and even to the optimization of chaotic systems themselves, for instance by maximizing the Kaplan–Yorke dimension [3,36], while the performance of GWO has been further enhanced through the integration of chaotic maps and hybridization strategies [37,38].

Notwithstanding this extensive progress, the systematic, optimization-based selection of closed-loop pole locations for the local stabilization of the Moore–Spiegel chaotic oscillator has received little attention. Existing GWO-based control studies predominantly target LQR weighting matrices or application-specific robotic and power-electronic systems, whereas optimization-based pole-placement studies have mostly relied on GA or PSO. A unified framework that couples analytic pole placement with GWO-driven pole selection (under an explicit cost function balancing transient performance and control energy, an explicit multi-scenario robustness criterion, and control-theoretic constraints) applied to a canonical chaotic benchmark, has not yet been reported.

This study addresses this gap by developing a GWO-based optimal pole-placement framework for the local stabilization of the Moore–Spiegel chaotic oscillator at the chaotic operating point $T = 36$ and $R = 100$. The main contributions are threefold: (i) a complete dynamical characterization that rigorously establishes the chaotic nature of the system through equilibrium and eigenvalue-based stability analysis, the phase-space divergence, the Lyapunov spectrum, the Kaplan–Yorke dimension, and a bifurcation study; (ii) the formulation of a composite cost function combining ITAE, ISE, and control-energy, overshoot, and settling-time penalty terms, minimized by the GWO under a minimax robustness criterion over three distinct initial conditions and subject to four control-theoretic constraints, with the feedback gain computed analytically through Ackermann's formula at every evaluation; and (iii) a comprehensive comparison against a conventional pole-placement baseline, together with robustness assessments under measurement noise and $\pm 10\%$ parametric uncertainty.

The remainder of the paper is organized as follows. Section 2 presents the Moore–Spiegel system and its detailed dynamical characterization, demonstrating that the system is chaotic. Section 3 describes the state-feedback controller, the GWO-based optimization framework, and the baseline controller. Section 4 reports the closed-loop optimization results and the robustness analyses. Section

CC: BY-NC-ND

5 discusses the findings, and Section 6 concludes the paper.

2. THE MOORE-SPIEGEL CHAOTIC SYSTEM

This section presents the Moore–Spiegel oscillator and characterizes its dynamics at the operating point considered throughout this study. The analysis combines equilibrium and local stability analysis, a dissipativity assessment based on the phase-space divergence, the Lyapunov spectrum, the Kaplan–Yorke fractal dimension, and a bifurcation study. Together, these results establish that the system is chaotic and provide the dynamical context for the controller design developed in Section 3.

2.1. System Description

The Moore–Spiegel oscillator is governed by the following set of first-order nonlinear ordinary differential equations given in Eq. (1):

$$\begin{aligned} \dot{x}_1 &= x_2 \\ \dot{x}_2 &= x_3 \\ \dot{x}_3 &= -x_3 - (T - R + Rx_1^2)x_2 - Tx_1 \end{aligned} \tag{1}$$

where x_1, x_2, and x_3 denote the position, velocity, and acceleration state variables, respectively; T is the thermal parameter; and R is the Rayleigh number. The nonlinearity enters through the amplitude-dependent coupling term $Rx_1^2x_2$, which makes the dynamics strongly sensitive to the magnitude of the oscillation. Throughout this study the parameter values $T = 36$ and $R = 100$ are adopted; the analyses presented below confirm that these values place the system in a chaotic regime.

Figure 1 shows the phase portraits obtained by numerical integration of the system, and Figure 2 presents the corresponding time series of the three state variables. The phase portraits reveal a bounded but non-repeating trajectory that traces out a strange attractor, while the time series display the aperiodic, irregular oscillations typical of chaotic motion.

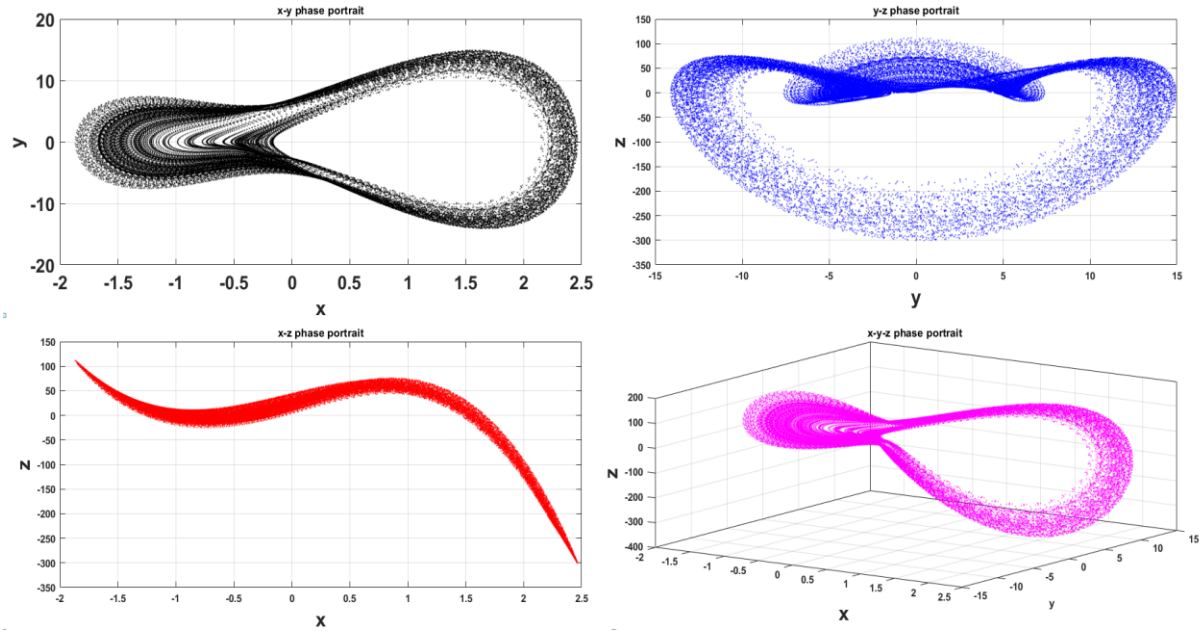

Figure 1. Phase portraits of the Moore–Spiegel chaotic system

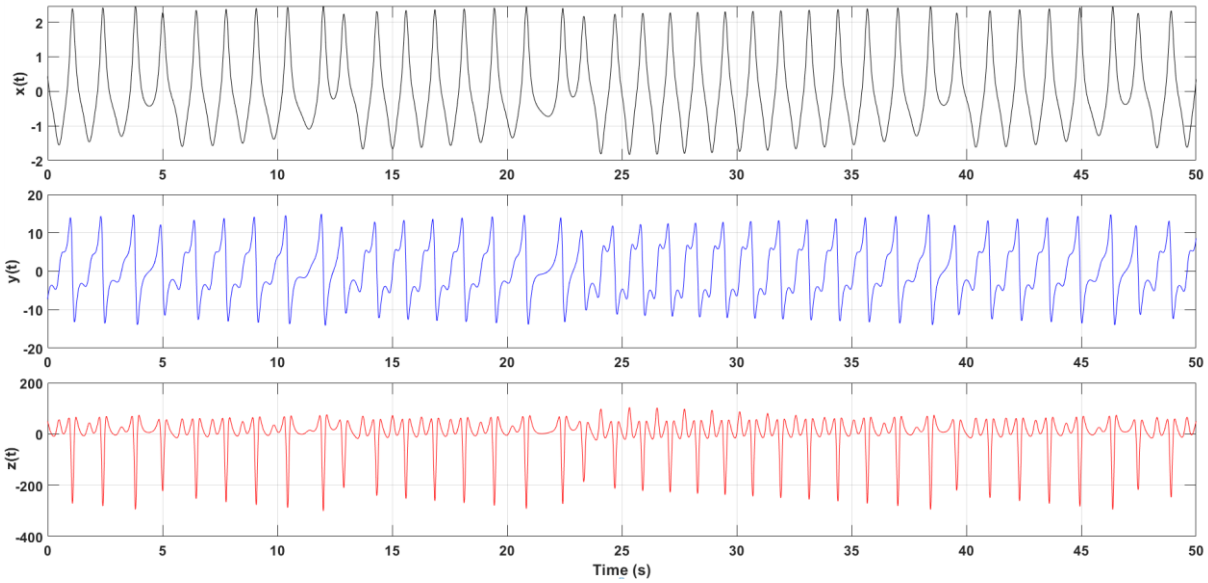

Figure 2. Time series of the Moore–Spiegel chaotic system

2.2. Equilibrium Point and Local Stability Analysis

The equilibrium points of the system are obtained from the conditions $\dot{x}_1 = \dot{x}_2 = \dot{x}_3 = 0$. The first two equations immediately give $x_2 = 0$ and $x_3 = 0$. Substituting these into the third equation yields Eq. (2):

$$-Tx_1 = 0 \tag{2}$$

Since T ≠ 0, the system possesses a single equilibrium point at the origin, given by Eq. (3):

$$x_e = E_0 = (0,0,0) \tag{3}$$

To examine the local stability of this equilibrium, the Jacobian matrix of the vector field is computed. With $J_{ij} = \frac{\partial f_i}{\partial x_j}$, the general Jacobian is given by Eq. (4):

$$J(x) = \begin{bmatrix} 0 & 1 & 0 \\ 0 & 0 & 1 \\ -T - 2Rx_1x_2 & -(T - R + Rx_1^2) & -1 \end{bmatrix} \tag{4}$$

Evaluating the Jacobian at the equilibrium point with $T = 36$ and $R = 100$ gives the linearization matrix in Eq. (5):

$$A = J(E_0) = \begin{bmatrix} 0 & 1 & 0 \\ 0 & 0 & 1 \\ -36 & 64 & -1 \end{bmatrix} \tag{5}$$

The eigenvalues of A are the roots of the characteristic equation $det(A - \lambda I) = 0$, which for this matrix is given by Eq. (6):

$$\lambda^3 + \lambda^2 - 64\lambda + 36 = 0 \tag{6}$$

The roots of this cubic are $\lambda_{J,1} = -8.7678$, $\lambda_{J,2} = +0.5705$, and $\lambda_{J,3} = +7.1973$. The presence of two eigenvalues with positive real part identifies the origin as an unstable, saddle-type equilibrium, which is consistent with the chaotic behaviour of the system: a saddle-type instability, in which eigenvalues of mixed sign coexist at the equilibrium, is a characteristic and necessary feature of systems that generate strange attractors [8,9]. The two positive eigenvalues correspond to a two-dimensional unstable manifold around the equilibrium, along which trajectories are repelled, whereas the single negative eigenvalue defines a one-dimensional stable direction. This combination of

repelling and attracting directions causes nearby trajectories to be stretched along the unstable manifold and folded back by the global nonlinearity, which is the mechanism underlying the system's sensitive dependence on initial conditions and chaotic behavior.

2.3. Dissipativity and Phase-Space Volume Contraction

The conservation properties of the system are assessed through the divergence of the vector field $F = (\dot{x}_1, \dot{x}_2, \dot{x}_3)$, which equals the trace of the Jacobian, as expressed in Eq. (7):

$$\nabla \cdot F = \frac{\partial \dot{x}_1}{\partial x_1} + \frac{\partial \dot{x}_2}{\partial x_2} + \frac{\partial \dot{x}_3}{\partial x_3} = trace(J) = 0 + 0 - 1 = -1 \tag{7}$$

Because the divergence is constant, negative, and nonzero, the system is not volume-preserving (conservative) but dissipative. According to Liouville's theorem, the time evolution of an infinitesimal phase-space volume obeys Eq. (8):

$$V(t) = V(0)e^{(\nabla \cdot F)t} = V(0)e^{-t} \tag{8}$$

Hence, a volume element selected in phase space contracts exponentially with time. This volumetric contraction is a necessary condition for the existence of a bounded attractor: although trajectories are locally repelled from the unstable equilibrium, the overall phase-space volume shrinks, so the motion is ultimately confined to a low-dimensional attracting set rather than diverging to infinity.

2.4. Lyapunov Exponents

The Lyapunov exponents quantify the average exponential rates at which infinitesimally close trajectories diverge from or converge to one another, and they provide the most direct quantitative test for chaos. An infinitesimal perturbation δx about a trajectory $x(t)$ evolves according to the variational (tangent linear) equation given in Eq. (9):

$$\delta \dot{x} = J\big(x(t)\big)\delta x \tag{9}$$

Introducing the fundamental solution matrix $\Phi(t)$, defined by $\dot{\Phi} = J(x(t))\Phi$ with $\Phi(0) = I$, the i-th Lyapunov exponent is defined as in Eq. (10):

$$\lambda_{\mathrm{i}} = lim(t \to \infty)(1/t) ln \sigma_{\mathrm{i}}(t) \tag{10}$$

where $\sigma_{\mathrm{i}}(t)$ are the singular values of $\Phi(t)$. In practice these exponents were computed by numerically integrating the augmented state–variational system together with a periodic QR re-orthonormalization of Φ, accumulating the logarithms of the diagonal elements of the upper-triangular factor; this Wolf-type procedure is the standard numerical method for estimating the Lyapunov spectrum of chaotic systems [7,11]. The resulting Lyapunov spectrum is given in Eq. (11):

$$\lambda_1 = 0.20111232, \lambda_2 = 0.00035110, \lambda_3 = -1.20146287 \tag{11}$$

The positive largest exponent confirms the exponential divergence of nearby trajectories and hence the sensitive dependence on initial conditions that is the defining feature of chaos; a positive largest Lyapunov exponent is the primary quantitative indicator that a system is chaotic [7,8]. The second exponent, being very close to zero, corresponds to the neutral direction expected along the flow of a continuous-time autonomous system, while the strongly negative third exponent reflects the dominant contracting direction. The signature $(+,0,-)$ is precisely the spectrum expected for a continuous-time chaotic flow.

As a consistency check, the sum of the Lyapunov exponents equals the phase-space divergence, as verified in Eq. (12):

$$\lambda_1 + \lambda_2 + \lambda_3 = -0.99999946 \approx \nabla \cdot F = -1 \tag{12}$$

The close agreement between the numerically obtained sum and the theoretical divergence value confirms both the dissipative nature of the system and the reliability of the numerical Lyapunov

CC: BY-NC-ND

computation. The convergence of the three Lyapunov exponents with integration time is shown in Figure 3, where the exponents settle to their asymptotic values, with one curve stabilizing at a positive level, one near zero, and one at a negative level.

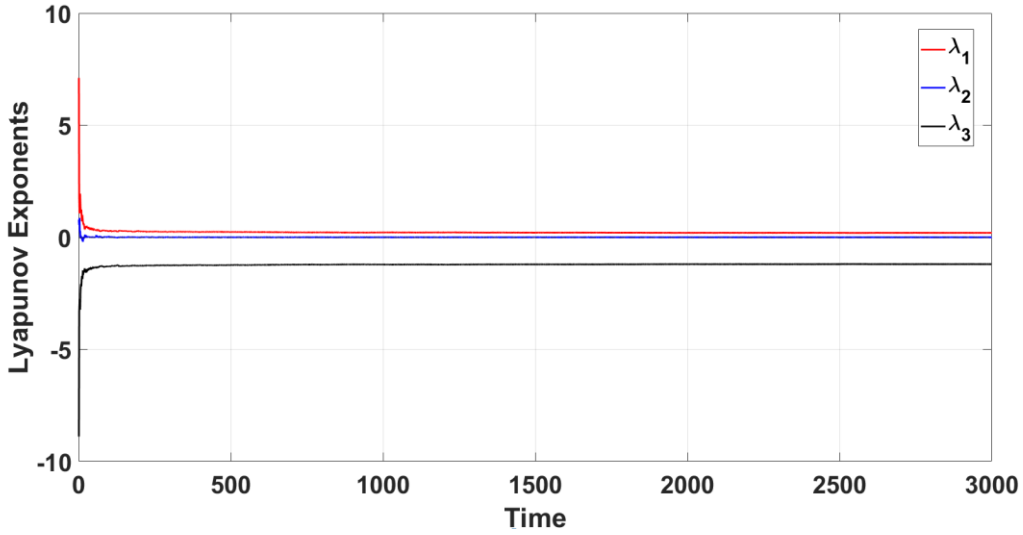

Figure 3. Convergence of the Lyapunov exponents (λ_1, λ_2, λ_3) of the Moore–Spiegel system as a function of integration time

2.5. Kaplan–Yorke Dimension

The fractal dimension of the attractor is estimated from the Lyapunov spectrum using the Kaplan–Yorke (Lyapunov) dimension. With the exponents ordered as $\lambda_1 \geq \lambda_2 \geq \lambda_3$, the Kaplan–Yorke dimension is defined as in Eq. (13):

$$D_{KY} = j + \frac{(\lambda_1+\lambda_2+\cdots+\lambda_j)}{|\lambda_{j+1}|} \tag{13}$$

where j is the largest integer for which the cumulative sum $\lambda_1 + \cdots + \lambda_j \geq 0$. For the present system the cumulative sums are:

$$s_1 = \lambda_1 = 0.20111232 > 0$$

$$s_2 = \lambda_1 + \lambda_2 = 0.20146342 > 0$$

$$s_3 = \lambda_1 + \lambda_2 + \lambda_3 = -0.99999946 < 0$$

so that $j = 2$. Substituting the numerical values gives, as shown in Eq. (14),

$$D_{KY} = 2 + \frac{(\lambda_1+\lambda_2)}{|\lambda_3|} = 2 + \frac{(0.20111232+0.00035110)}{1.20146287} = 2.16768176 \tag{14}$$

The non-integer Kaplan–Yorke dimension confirms that the attractor possesses a fractal geometric structure, the Lyapunov (Kaplan–Yorke) dimension being a standard measure of the fractal dimension of a strange attractor obtained directly from the Lyapunov spectrum [7]. Its value between 2 and 3 indicates an object that is more complex than a two-dimensional surface but that does not fill the entire three-dimensional phase volume, consistent with the strange attractor observed in the phase portraits of Figure 1.

2.6. Bifurcation Analysis

To place the operating point within the global dynamical landscape of the system, a bifurcation diagram was constructed by recording the asymptotic local maxima of the state variable x_1 while the thermal parameter T was varied, with the Rayleigh number held fixed at $R = 100$. The resulting diagram is shown in Figure 4.

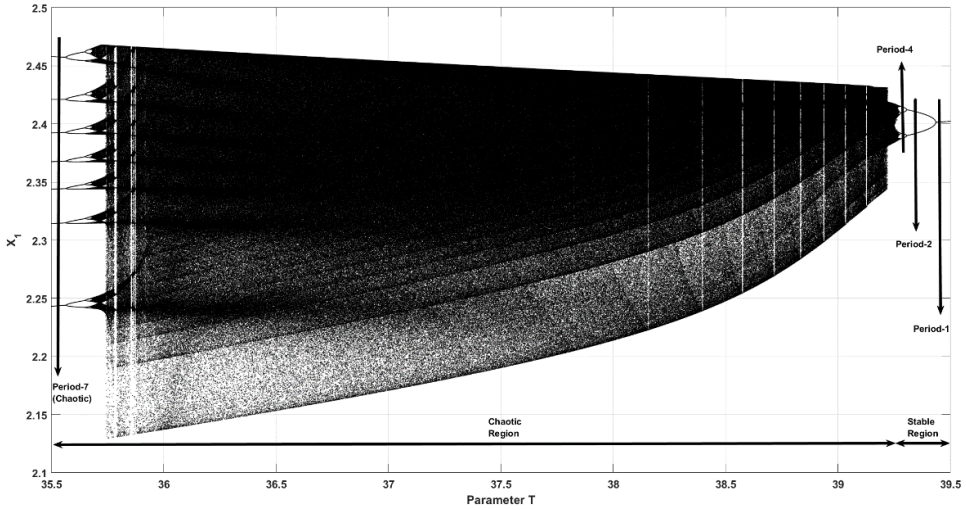

Figure 4. Bifurcation diagram of the Moore–Spiegel system with respect to the thermal parameter T ($R = 100$), showing the chaotic region, periodic windows, and the period-doubling structure

The bifurcation diagram reveals a broad chaotic region over the lower range of T, within which the operating point $T = 36$ used in this study is located. In this region the recorded maxima form a dense band of values, indicating aperiodic motion, interrupted by narrow periodic windows. As T increases toward the upper end of the range, the system undergoes a reverse period-doubling (period-halving) cascade, passing successively through period-4, period-2, and period-1 behavior before settling into a stable, periodic region. This period-doubling structure is one of the classical routes to chaos and is among the bifurcation phenomena previously documented for the Moore–Spiegel system [6,8]; it further confirms that, at $T = 36$, the Moore–Spiegel system operates well inside the chaotic regime.

Taken together, the unstable saddle-type equilibrium, the negative phase-space divergence, the Lyapunov spectrum of signature $(+,0,-)$ with a positive largest exponent, the non-integer Kaplan–Yorke dimension, and the bifurcation structure provide consistent and mutually reinforcing evidence that the Moore–Spiegel system is chaotic at the chosen parameter values. This chaotic, dissipative system is the plant to be stabilized by the controller developed in the following section.

3. CONTROLLER DESIGN AND OPTIMIZATION FRAMEWORK

This section develops the proposed controller in four parts, each presented in a dedicated subsection. Section 3.1 formulates the single-input state-feedback controller obtained from the linearized model of the Moore–Spiegel system and verifies its controllability. Section 3.2 casts the selection of the closed-loop poles as an optimization problem, introducing the composite multi-term cost function (combining ITAE, ISE, control energy, overshoot, and settling time), the minimax robustness strategy over multiple initial conditions, and the control-theoretic constraints enforced through a penalty-based approach. Section 3.3 summarizes the Grey Wolf Optimizer and its parameter settings, and Section 3.4 describes the conventional pole-placement controller adopted as a baseline for comparison.

3.1. State-Feedback Controller Design

Since the control input can be applied only through the acceleration channel, the input matrix is defined as $B = [0,0,1]^{\mathrm{T}}$. Because the control input u is scalar, the feedback law $u(t) = -K(x - x_{\mathrm{e}})$ employs a feedback gain K that is a 1×3 row vector rather than a matrix. The controllability matrix $C = [B, AB, A^2B]$ has full rank 3, confirming that the linearized system is completely controllable and that arbitrary pole placement is therefore feasible; verifying the full rank of the controllability matrix is the standard prerequisite that guarantees a solution to the pole-placement problem [14,15].

The closed-loop system dynamics can be written as in Eq. (15):

CC: BY-NC-ND

$$\dot{x} = (A - BK)(x - x_e) + f_{nl}(x) \tag{15}$$

where $f_{nl}(x)$ denotes the nonlinear residual term, which vanishes at the equilibrium point. Owing to the design being based on Jacobian linearization, the proposed controller provides local stabilization only within the region of validity of the linearized model.

3.2. GWO-Based Optimal Pole Placement

Rather than selecting the closed-loop pole locations heuristically, the Grey Wolf Optimizer is used to determine, in a systematic manner, the optimal pole locations that minimize a composite performance index. The decision-variable vector is defined as $p = [\sigma, \omega, \sigma_3]^{\mathrm{T}}$, from which three desired closed-loop poles are constructed as $-\sigma \pm j\omega$ and $-\sigma_3$. The feedback gain vector K is computed at every function evaluation using Ackermann's formula [39].

3.2.1. Composite Cost Function

A weighted composite cost function that simultaneously addresses transient tracking accuracy, control-energy consumption, overshoot, and settling behavior is defined as in Eq. (16). For each initial condition, the scenario cost is:

$$J = w_1 \cdot ITAE_i + w_2 \cdot ISE_i + w_3 \cdot E_{u,i} + w_4 \cdot O_i + w_5 \cdot T_{s,i} \tag{16}$$

Here, ITAE penalizes slowly settling responses, ISE penalizes large error deviations, the control-energy term (integral of the squared control input) discourages excessive actuator effort, the overshoot term O penalizes any growth of the error norm beyond its initial value, and the settling-time term Ts penalizes late entry into the 2% band. The error is defined as $e = x - xe$, all terms are evaluated over a 15-second ($t = 15\ s$) simulation horizon for each of the three initial conditions, and the overall objective is the minimax (worst-case) value across them, as given in Eq. (18). The weighting coefficients are set to $w_1 = 0.40$ and $w_2 = 0.20, w_3 = 0.10, w_4 = 0.15$ and $w_5 = 0.15$. The five coefficients sum to unity and were fixed on the basis of preliminary simulations rather than being tuned during the optimization itself. The largest share is assigned to ITAE, which is adopted as the principal transient-accuracy criterion; a smaller share is given to ISE, whose magnitude is already large for the chaotic transients considered; and the remaining share is distributed between the control-energy, overshoot and settling-time terms, which act mainly as shaping penalties that discourage aggressive, high-gain placements. Because ITAE and ISE differ both in numerical scale and in physical meaning, the influence of this weighting on the resulting optimum was not assumed but was quantified explicitly through the weight-sensitivity study reported in Section 4.2.

3.2.2. Minimax Robustness Strategy

To ensure that the optimized controller performs adequately under different operating conditions, a minimax strategy is adopted over three distinct initial conditions given in Eq. (17):

$$x_0^{(1)} = [0.5; 0.2; -0.3]^{\mathrm{T}}, x_0^{(2)} = [1.5; 0.5; -1.0]^{\mathrm{T}}, x_0^{(3)} = [2.0; -1.0; 1.5]^{\mathrm{T}} \tag{17}$$

$$J_{minimax} = max\ \left\{J\left(x_0^{(1)}\right), J\left(x_0^{(2)}\right), J\left(x_0^{(3)}\right)\right\} \tag{18}$$

The minimax objective in Eq. (18) prevents the optimization from selecting pole locations that perform well for a single initial condition but fail for others, thereby promoting robust performance within the local stabilization region. The three conditions were selected so as to span the local operating region of interest with increasing severity rather than to represent a single nominal operating point: the initial state-error norms are 0.62, 1.87 and 2.69 for $x_0^{(1)}$, $x_0^{(2)}$ and $x_0^{(3)}$, respectively, so that $x_0^{(1)}$ is a small perturbation about the equilibrium, $x_0^{(2)}$ an intermediate one, and $x_0^{(3)}$ the most demanding of the three. All three lie inside the region of attraction of the linearization-based controller; this is confirmed a posteriori by the per-condition closed-loop responses reported later in the robustness analysis (Section 4.4), where the response obtained from each initial condition individually is shown to converge monotonically to the origin.

CC: BY-NC-ND

3.2.3. Constraint Handling

Four inequality constraints are imposed through a penalty-based approach:

• $\omega < \sigma$: guarantees a damping ratio $\zeta = \sigma/\sqrt{(\sigma^2 + \omega^2)} > 0.707$, thereby preventing strongly oscillatory transient behavior.

• $\sigma \leq \sigma_3 \leq 3\sigma$: keeps the real pole close to the dominant complex pole pair.

• $\omega_n \leq$ 30 rad/s: limits the natural frequency to prevent excessively large feedback gains.

• $Re(\lambda max) < -1$: enforces a minimum closed-loop stability margin beyond the linearization threshold.

3.3. Grey Wolf Optimizer

The GWO algorithm proposed by Mirjalili et al. [22] is a population-based metaheuristic inspired by the social hierarchy and hunting behavior of grey wolves. The algorithm designates the three best solutions found so far as Alpha (α), Beta (β), and Delta (δ), which guide the search performed by the remaining individuals (ω). The position-update equations are given in Eqs. (19) and (20):

$$\begin{aligned} X_1 &= X\alpha - A_1 \cdot |C_1 \cdot X\alpha - X| \\ X_2 &= X\beta - A_2 \cdot |C_2 \cdot X\beta - X| \\ X_3 &= X\delta - A_3 \cdot |C_3 \cdot X\delta - X| \end{aligned} \tag{19}$$

$$X(t+1) = \frac{(X_1 + X_2 + X_3)}{3} \tag{20}$$

The coefficient vectors are computed as $A = 2a \cdot r_1 - a$ and $C = 2r_2$, where r_1 and r_2 are random vectors in $[0, 1]$ and the parameter a decreases linearly from 2 to 0 over the course of the iterations, balancing exploration and exploitation. The control parameters used for the GWO are listed in Table 1.

Table 1. Parameter settings of the Grey Wolf Optimizer

Parameter	**Value**
Number of search agents (N)	50
Maximum number of iterations	300
Maximum function evaluations	15,000
Number of independent runs	30
Number of leaders (α, β, δ)	3
Coefficient a (start → end)	2 → 0 (linear)
Decision-variable dimension	3 $[\sigma, \omega, \sigma_3]$
Search-space lower bounds [lb]	[1.1 ; 0.01 ; 1.1]
Search-space upper bounds [ub]	[15 ; 14 ; 45]

The population size and the computational budget follow common practice for low-dimensional continuous problems and are consistent with the settings adopted in the original GWO study [22] and in subsequent control applications [28,31]. With only three decision variables, 50 search agents provide adequate coverage of the search space, while 300 iterations (15,000 function evaluations) exceed by a wide margin the budget actually required for convergence, which Figure 5 shows to be reached within the first few tens of iterations; the surplus budget therefore acts as a safeguard rather than as an active limitation. The same budget of 15,000 function evaluations was imposed on PSO and

CC: BY-NC-ND

GA so that the three algorithms are compared under identical conditions, and 30 independent runs were performed so that the best, mean, worst, median and standard-deviation statistics reported in Table 2 are statistically meaningful. The search-space bounds were deliberately kept wide so as not to constrain the optimum artificially. The lower bounds in particular were relaxed relative to a preliminary configuration, so that the optimizer is free to explore small-magnitude pole locations. As shown in Section 4.2, the resulting optimum lies in the interior of this box and is not active at any bound; the binding constraints are instead the damping requirement ($\omega < \sigma$, i.e. $\zeta >= 0.707$) and the stability-margin requirement, both enforced through the penalty terms of the cost function. The upper bounds were chosen to preclude excessively large feedback gains, which would violate the local validity of the linearization and risk actuator saturation.

3.4. Reference Controller

For comparative evaluation, a baseline controller was designed using conventional pole placement without optimization, following the classical eigenvalue-assignment formulations that underpin state-feedback design [17,18]. The closed-loop poles were placed at $-8 \pm 7j$ and −8.5, yielding the corresponding feedback gain vector $K_{ref} = [924.5,313.0,23.5]$. In this design the dominant poles are positioned close to the largest unstable open-loop mode ($\lambda_{J,3} = +7.20$), with a damping ratio $\zeta = 8/\sqrt{(8^2 + 7^2)} = 0.753$ and a natural frequency $\omega_n = 10.63$ rad/s. This approach represents a naive engineering choice in which the designer fixes the poles heuristically, without regard to any performance criterion or systematic optimization.

4. RESULTS

This section reports the results obtained with the proposed framework, organized into four subsections. Section 4.1 examines the convergence behaviour and reproducibility of the Grey Wolf Optimizer over 30 independent runs. Section 4.2 presents the optimized controller parameters together with the resulting closed-loop pole locations. Section 4.3 compares the transient performance of the optimized and baseline controllers through quantitative metrics and time-domain responses. Finally, Section 4.4 assesses the robustness of the optimized controller under measurement noise, parametric uncertainty, and variation of the initial condition.

4.1. GWO Convergence Analysis

GWO, PSO, and GA were each executed over 30 independent runs of 300 iterations (MaxFEs = 15,000) on the same problem and search space, to verify that the optimal solution is algorithm-independent. The convergence statistics are summarized in Table 2.

Table 2. Convergence statistics of GWO, PSO, and GA over 30 independent runs (same problem, bounds, and 15,000-FE budget).

Algorithm	Best	Mean	Std. Deviation	Worst	Median
GWO	353.14	353.63	0.218	353.73	353.73
PSO	353.73	353.73	0.002	353.73	353.73
GA	354.12	355.60	0.939	357.83	355.65

As shown in Figure 5, the cost function decreased by approximately an order of magnitude within the first ten iterations and reached a stable plateau around the twentieth iteration. This rapid convergence indicates that the feasible region within the defined search space is exploited efficiently by the GWO. The small standard deviations reported in Table 2 (0.218 for GWO, 0.002 for PSO, and 0.939 for GA) reveal that all three algorithms converged to essentially the same solution across the 30 independent runs, indicating that the located optimum is algorithm-independent rather than an artefact of any single method.

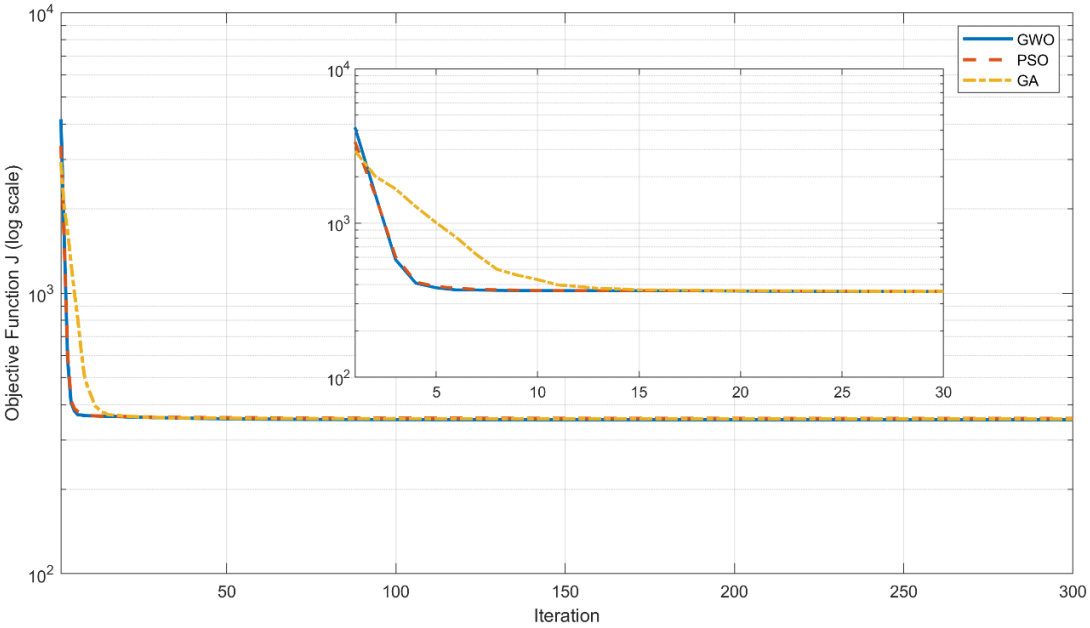

Figure 5. Mean convergence curves of GWO, PSO, and GA (30 independent runs each; logarithmic scale, with a zoomed inset over the first iterations)

The box plot in Figure 6 compares the objective-function distributions of the three algorithms; GWO and PSO are tightly concentrated at the optimum while GA shows a slightly wider spread, yet all three converge to essentially the same value. This demonstrates both the reproducibility of the framework and the algorithm-independence of the optimum. The near-coincident statistical measures for GWO and PSO further support this conclusion.

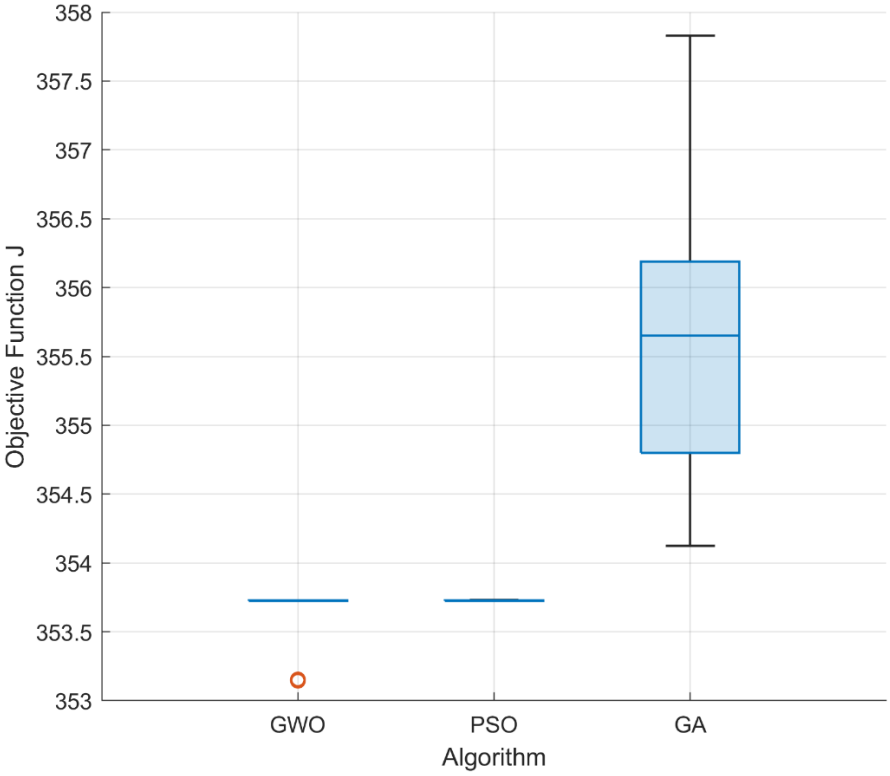

Figure 6. Distribution of the objective-function value for GWO, PSO, and GA over 30 independent runs

CC: BY-NC-ND

4.2. Optimized Controller Parameters

The best solution found by the GWO lies in the interior of the search space. The optimum is not active at any bound; the pole-parameter vector obtained is $p^* = [\sigma = 3.0016; \omega = 3.0015; \sigma_3 = 3.0519]^T$. The feedback gain vector obtained through Ackermann's formula is $K_{opt} = [18.9901, 100.3393, 8.0550]$. Table 3 compares the key parameters of the baseline and optimized controllers.

Table 3. Comparison of the baseline and the GWO-, PSO-, and GA-optimized controller parameters

Method	K_1	K_2	K_3	ζ	w_n $(\frac{rad}{s})$
Baseline (pole placement)	924.5	313.0	23.5	0.753	10.63
Optimized (GWO)	18.9901	100.3393	8.0550	0.7071	4.24
Optimized (PSO)	18.9731	100.3236	8.0541	0.7071	4.24
Optimized (GA)	19.4629	100.6964	8.1457	0.7147	4.25

As seen in Figure 7, the GWO-, PSO-, and GA-optimized poles cluster together at the same interior location, corresponding to a well-damped configuration ($\zeta = 0.707$). In contrast, the baseline poles (orange circles) form a complex pair with significant imaginary components ($\zeta = 0.753$). While maintaining a damping ratio at the design threshold ($\zeta = 0.707$), the optimized controller reduces the feedback-gain magnitudes by more than a factor of forty relative to the baseline (e.g. K_1 from 924.5 to 19.0), which is the dominant source of the large reductions in control energy and overshoot reported below.

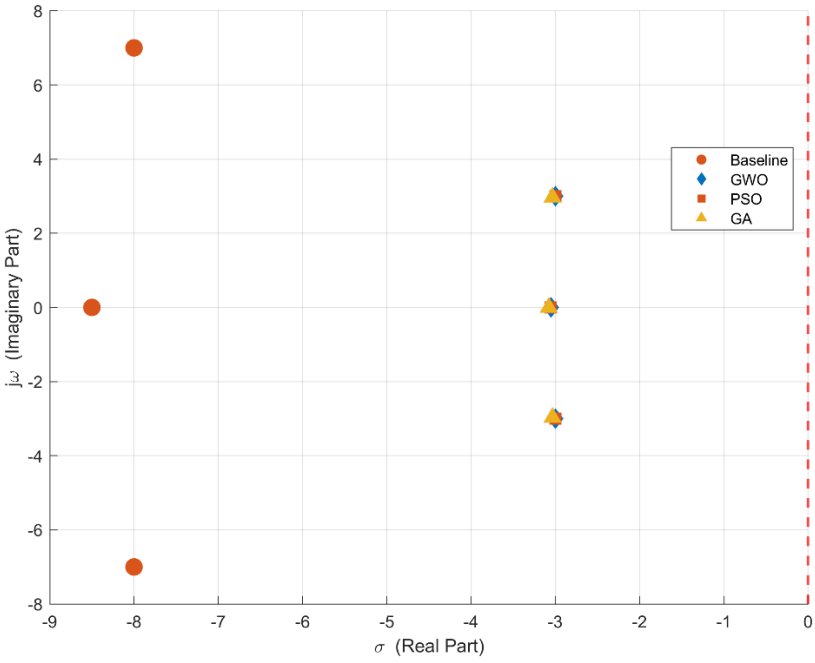

Figure 7. S-plane: closed-loop pole locations of the baseline and the GWO-, PSO-, and GA-optimized controllers

To confirm that the optimum is not an artefact of the particular cost-function weights, a sensitivity analysis was carried out in which the ITAE weight w1 was varied over {0.30, 0.40, 0.50} while the remaining weights were rescaled to preserve a unit sum. As summarized in Table 4, the optimal pole configuration is essentially invariant to this variation: the damping ratio remains fixed at $\zeta = 0.7071$ and the gain vector changes by only about one per cent across the range. The solution is therefore dictated by the damping and stability-margin constraints rather than by the specific

numerical values of the weights.

Table 4. Sensitivity of the optimal pole configuration to the ITAE weight w_1.

w_1 (ITAE weight)	$(\sigma, \omega, \sigma_3)$	ζ	w_n	$K = [K_1, K_2, K_3]$
0.30	(3.002, 3.002, 3.042)	0.7071	4.245	[18.81, 100.28, 8.05]
0.40	(3.002, 3.002, 3.052)	0.7071	4.245	[18.9901, 100.3393, 8.0550]
0.50	(3.000, 3.000, 3.062)	0.7071	4.242	[19.11, 100.37, 8.06]

4.3. Control Performance Comparison

Table 5 presents the performance metrics averaged over the three minimax initial conditions. Figures 8–11 provide the corresponding visual evidence. Here overshoot is defined relative to the initial state-error norm (the peak of the error norm relative to its initial value), rather than as tracking overshoot about a non-zero reference; this is the natural definition for a regulation-to-origin problem and explains the large percentage values, which reflect the transient excursion of the chaotic state before stabilization.

Table 5. Performance metrics of the baseline and GWO-optimized controllers, averaged over the three minimax initial conditions

Metric	Baseline	Optimized (GWO)	Improvement (%)
ITAE	1.833	7.538	-311.3 (worse)
ISE	78.25	12.60	+83.9
IAE	5.868	4.900	+16.5
Settling time (s)	1.144	4.628	-304.5 (worse)
Overshoot (%)	1731.3	353.6	+79.6
Control energy	49,494.9	2,564.6	+94.8

These results reveal a deliberate trade-off induced by the five-term minimax cost function. Relative to the baseline, the optimized controller markedly reduces control energy (+94.8%), ISE (+83.9%), and overshoot (+79.6%), because its poles are placed at a moderate magnitude rather than deep in the left half-plane. The same choice, however, yields a slower settling time and a larger ITAE (both reported as negative improvements), since the dominant closed-loop mode is intentionally less aggressive than the baseline placement at $\sigma = 8$. This behaviour is expected and, indeed, desirable for a chaotic system whose linearization is only locally valid: a lower-gain, well-damped controller keeps the trajectory within the region where the linear model applies while avoiding the very large control effort of the baseline. This trade-off is therefore reported explicitly alongside the improvements, both here and in the abstract and the conclusion. It should be noted that the ITAE value reported in Table 5 (7.538 s) is the mean over the three minimax initial conditions, whereas the nominal-case ITAE listed in the robustness analysis (Table 6, 6.463 s) is evaluated for the single reference initial condition x0(2) used throughout the parametric-uncertainty study. The two quantities are computed over different sets of initial conditions and are therefore not expected to coincide: since ITAE increases monotonically with the initial state-error norm, the most demanding initial condition x0(3) raises the three-condition average above the value obtained for the intermediate reference condition, which fully accounts for the difference between the two tables.

Figure 8 shows that the open-loop trajectory forms a strange attractor within the range $|x_3| \leq 200$. Both closed-loop controllers successfully suppress the chaotic motion and drive the state toward the origin. The GWO-optimized trajectory exhibits a tighter phase-space trace than the baseline, in agreement with its lower ISE value in Table 5.

CC: BY-NC-ND

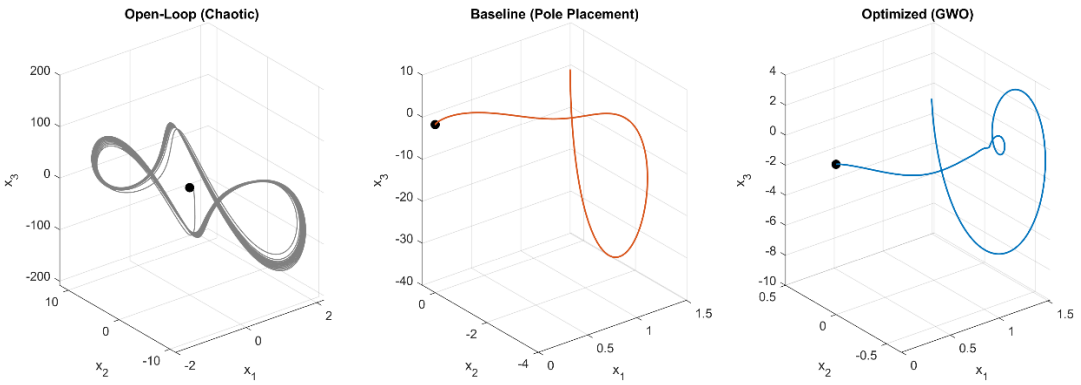

Figure 8. Three-dimensional phase-space portraits

Figure 9 shows that the open-loop system exhibits sustained chaotic oscillation with an error norm bounded by approximately 200. The optimized controller (blue) attains a markedly lower initial peak in the error norm than the baseline (orange), whose aggressive, oscillatory placement produces a much larger transient excursion; both closed-loop responses then drive the error norm to a negligible level within the first few seconds.

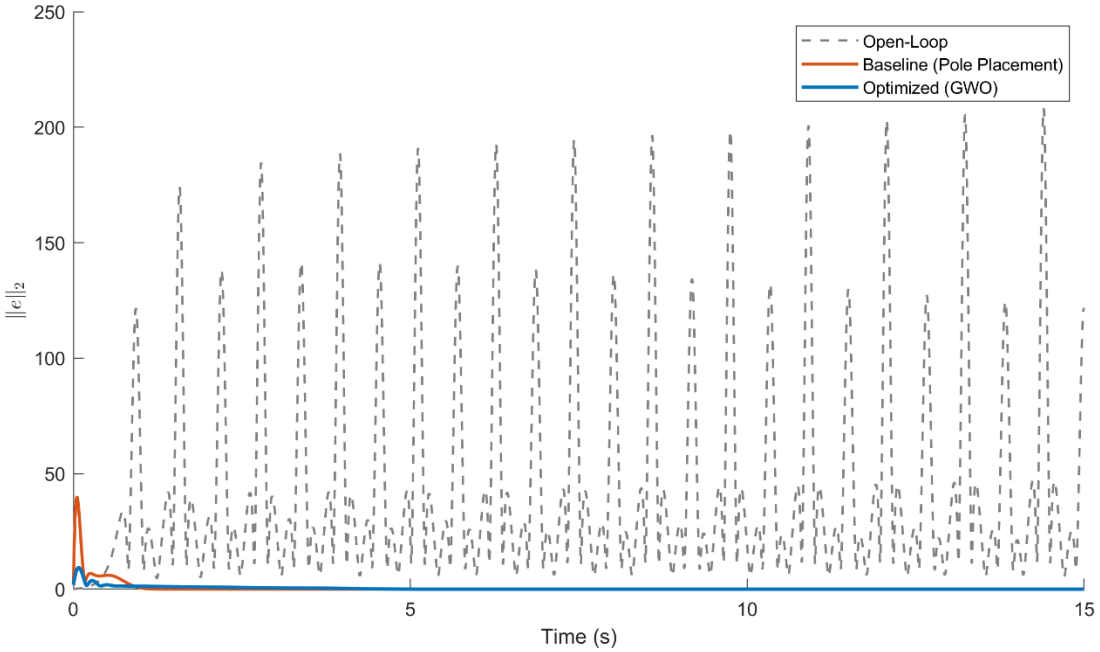

Figure 9. State error norm $\|x - x_e\|$ time history: open-loop (chaotic), baseline, and GWO-optimized controllers

The state trajectories in Figure 10 explain the improvements in the ISE and overshoot metrics. The baseline controller's $x_1(t)$ response decays rapidly but at the price of a pronounced transient excursion in the velocity and acceleration states, whereas the GWO-optimized controller produces a one-sided, monotonically decreasing response in all three state variables. The 79.6% reduction in overshoot is consistent with this visual evidence and is of practical importance for actuator saturation and mechanical fatigue. The longer settling time is a direct consequence of the 2% band criterion adopted here, and the higher ITAE follows from the same mechanism, since ITAE weights the error by the instant at which it occurs: the well-damped, moderate-gain response approaches the origin more gradually and therefore crosses this band later than the aggressive oscillatory baseline, but it does so monotonically and without ringing. As emphasized above, this slower settling is an intentional consequence of the lower-energy design.

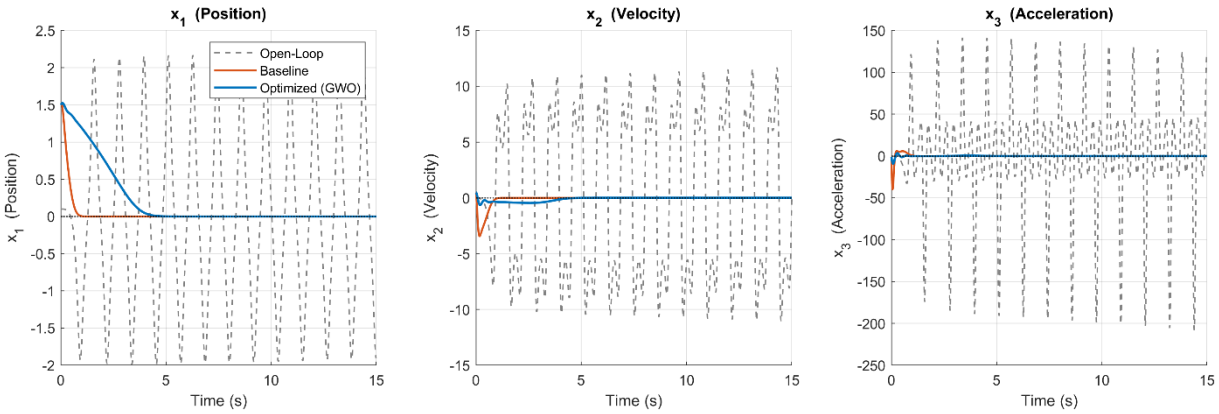

Figure 10. State-variable time histories

The control-input comparison in Figure 11 shows that the baseline controller produces a high initial control effort, reaching approximately −1600 at $t = 0$, whereas the initial control input of the GWO-optimized controller remains around 60 in magnitude. Both controllers drive the control input to near zero within about five seconds. The 94.8% reduction in control energy indicates that the optimized solution offers significant practical advantages for actuator design and energy efficiency.

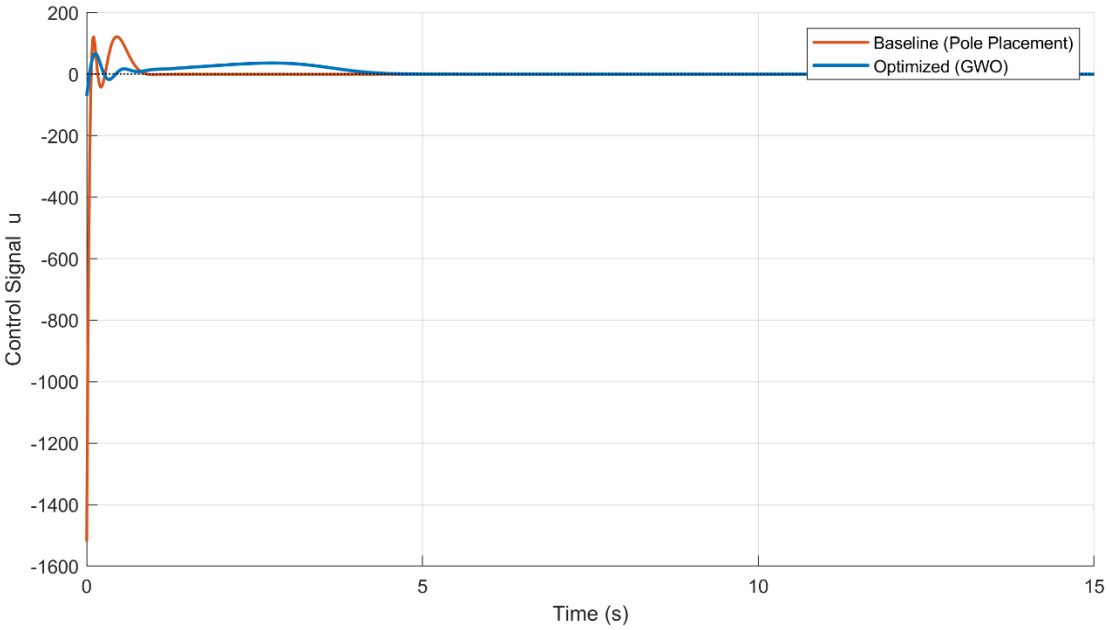

Figure 11. Control-input $u(t) = -K(x - x_e)$time history: baseline versus GWO-optimized controller

4.4. Robustness Analysis

4.4.1. Robustness to Measurement Noise

The sensitivity of the optimized controller to measurement noise was evaluated by adding proportional white noise at levels of 0%, 1%, 5%, and 10% to the state-feedback signal. As shown in Figure 12, the optimized controller maintained stable convergence at all tested noise levels. Even at 10% noise, only a marginal degradation of the transient behavior was observed, and for levels up to 5% the error-norm curves are nearly indistinguishable. This result indicates that the well-damped pole configuration exhibits inherent robustness to measurement uncertainty.

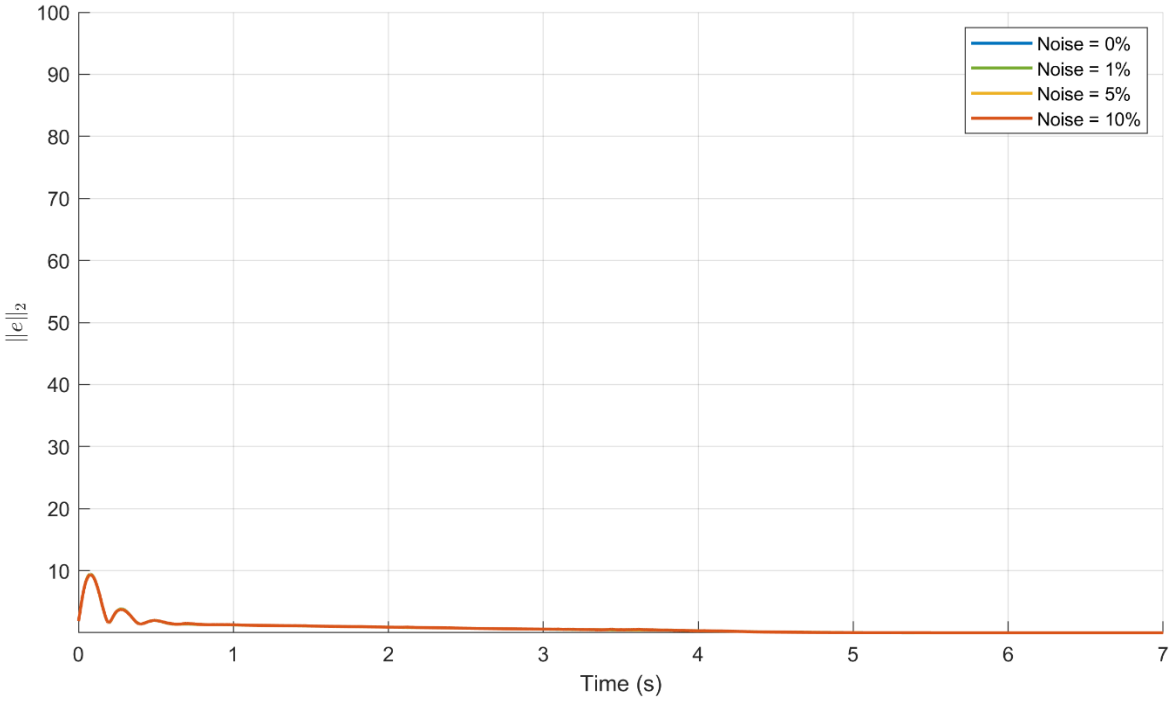

Figure 12. State error norm under measurement noise: optimized controller K evaluated at four noise levels

4.4.2. Robustness to Parametric Uncertainty

The robustness of the optimized controller to model-parameter variations was assessed by independently perturbing the thermal parameter T and the Rayleigh number R by $\pm 10\%$ about their nominal values ($T = 36, R = 100$). The results are summarized in Table 6.

Table 6. Robustness analysis under parametric uncertainty

Scenario (dT, dR)	ITAE	Stable?
T -10%, R -10%	6.791	Yes
T -10%, R +/-0%	6.908	Yes
T -10%, R +10%	8.729	Yes
T +/-0%, R -10%	6.441	Yes
T +/-0%, R +/-0% (nominal)	6.463	Yes
T +/-0%, R +10%	7.594	Yes
T +10%, R -10%	6.146	Yes
T +10%, R +/-0%	6.143	Yes
T +10%, R +10%	6.799	Yes

Table 6 and Figure 13 show that the optimized controller preserved closed-loop stability in all nine perturbation scenarios. The ITAE values ranged from 6.14 to 8.73, with a maximum deviation of 35.1% relative to the nominal case. This result confirms that the proposed GWO-based controller possesses satisfactory robustness to $\pm 10\%$ model uncertainty in both system parameters.

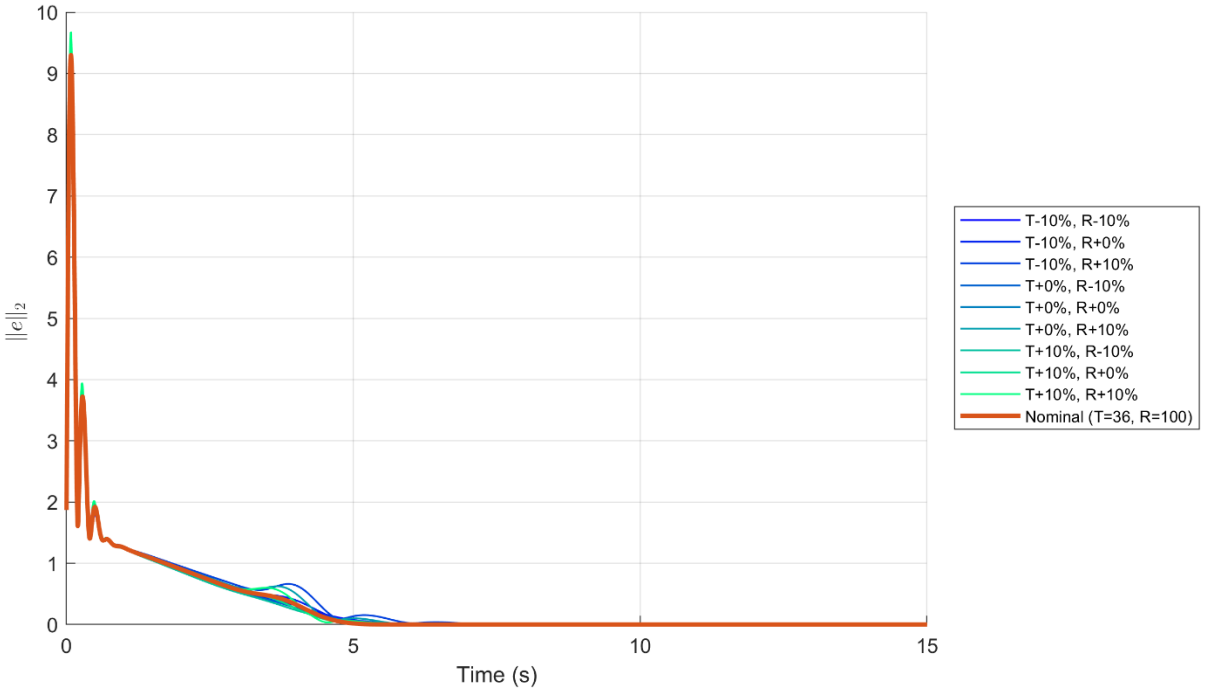

Figure 13. State error norm under parametric uncertainty: nominal case and eight scenarios with T and R perturbed by $\pm 10\%$

Since the controller is obtained from a minimax formulation over three initial conditions, its behaviour was finally examined for each of these conditions separately. Figure 14 reports the resulting closed-loop responses: the upper row shows the state-error norm on a logarithmic scale together with the 2% band, and the lower row the corresponding position response $x_1(t)$. In every scenario the error norm decays monotonically and enters the 2% band without ringing, at progressively later instants as the initial perturbation grows (approximately 2.8 s, 4.8 s and 6.3 s for $x_0^{(1)}$, $x_0^{(2)}$ and $x_0^{(3)}$, respectively), which is consistent with the mean settling time of 4.628 s reported in Table 5. The position responses are one-sided in all three cases and exhibit no overshoot about the equilibrium. These results confirm that all three conditions lie within the region of attraction of the linearization-based controller, and that the minimax formulation yields a design whose performance degrades gracefully as the initial perturbation grows rather than one tuned to a single operating point.

CC: BY-NC-ND

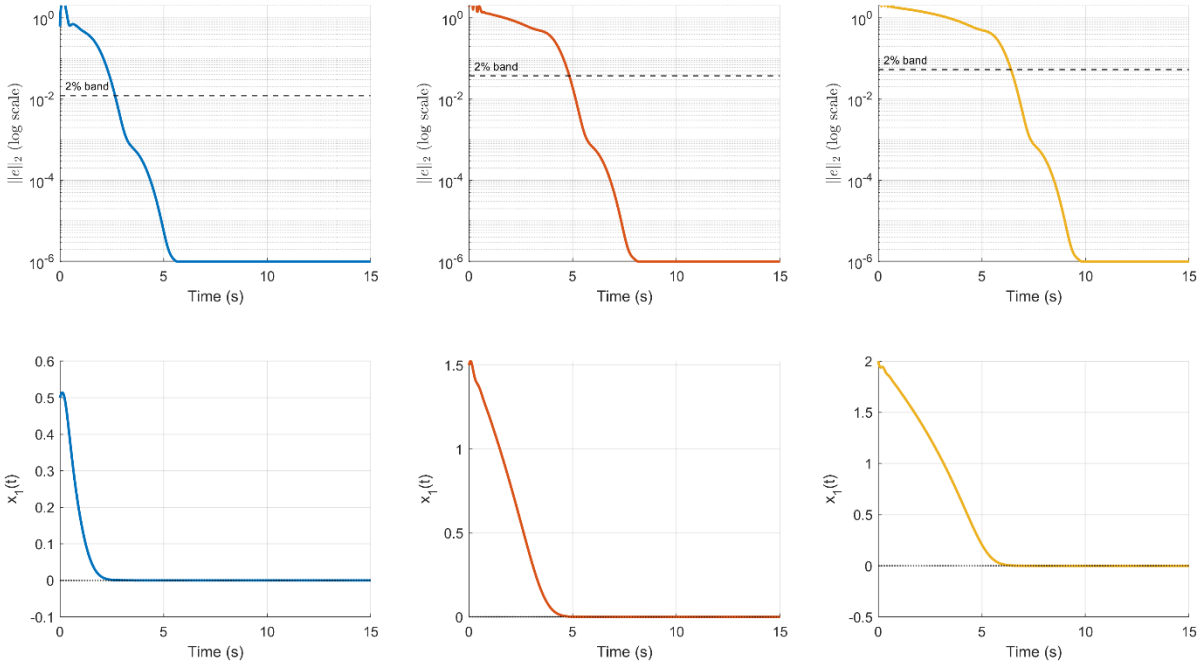

Figure 14. Closed-loop response of the GWO-optimized controller for each of the three minimax initial conditions (left: x0(1), middle: x0(2), right: x0(3)); upper row: state-error norm on a logarithmic scale with the 2% band, lower row: position response x1(t)

5. DISCUSSION

The proposed framework decouples the analytic and the search components of controller design: the pole-placement computation is carried out exactly through Ackermann's formula [39], while the selection of the desired pole locations is delegated to the GWO. Because the system is single-input ($B = [0,0,1]^T$), the feedback gain is a 1×3 row vector, and the optimization is conducted in a three-dimensional space defined through the physical pole parameters rather than over the gain entries directly; this parameterization inherently respects control-theoretic requirements such as conjugate symmetry and stability. The strategy is consistent with the broader literature in which metaheuristics replace the trial-and-error tuning that limits classical pole placement and LQR design [19-21]: genetic algorithms have been used to compute LQR weighting matrices automatically [21], and particle swarm optimization has been applied to LQR weight selection for oscillatory current controllers [20]. The present results extend this line of work by showing that the same philosophy transfers effectively to the local stabilization of a chaotic oscillator.

Relative to the conventional pole-placement baseline, the GWO-optimized controller reduced the ISE by 83.9%, the IAE by 16.5%, the overshoot by 79.6%, and the control energy by 94.8%, while reducing the dominant feedback gain by more than a factor of forty. These gains are in line with comparative findings reported across GWO-based control studies. Sun et al. obtained a GWO-tuned state-feedback controller that outperformed both a conventional state-feedback design and a genetic-algorithm-enhanced PI controller, achieving a faster response with no overshoot once a penalty term was incorporated into the cost index [28]; this mirrors the low-overshoot, energy-efficient response obtained here. In a similar vein, GWO outperformed PSO in sliding-mode quadrotor control [33] and converged faster than ACO, GA, and PSO in robust H∞ control of an underwater vehicle-manipulator system [32], while GWO-optimized feedback-linearization controllers preserved their performance both with and without disturbances [31]. The 94.8% reduction in control energy reported here is particularly relevant in this context, since lower actuator effort directly improves energy efficiency and reduces the risk of actuator saturation and mechanical fatigue. Beyond the present stabilization setting, the deliberate control of chaotic dynamics has likewise been demonstrated in practical mechatronic and robotic systems (for instance, chaotic position control to improve the stirring performance of a magnetic stirrer [40], and chaotic speed control of a DC motor based on the Sprott-A

system for robotic end-effector applications [41]) which together underscore the broader engineering relevance of systematically controlling chaotic systems such as the one addressed here.

The results in Table 5 also expose the trade-off between overshoot suppression and the formal settling time under the adopted cost function. By placing the closed-loop poles at a moderate, well-damped configuration (ζ = 0.707), the optimized controller produces a one-sided, ringing-free response in the state variables; however, the suppression of oscillation, combined with the comparatively low natural frequency of the optimized design (4.24 rad/s against 10.63 rad/s for the baseline), implies a gradual asymptotic approach to equilibrium, which lengthens both the ITAE and the settling time measured under the 2% band. This behaviour is fully consistent with classical linear control theory, in which a well-damped placement gives the fastest non-oscillatory response, whereas a more aggressive, lightly damped placement can score better on settling-time metrics at the price of ringing and a substantially larger control effort. The literature points to a natural remedy: because metaheuristic frameworks let the designer encode the desired transient explicitly, performance specifications such as settling time, rise time, steady-state error, and overshoot can be embedded as distinct objectives, as demonstrated in firefly-based and related optimization formulations [19]. Augmenting the composite cost with a settling-time term is therefore a promising direction for future work.

The minimax formulation over three distinct initial conditions is a central feature of the proposed method. Unlike single-scenario optimization, it explicitly seeks controllers that perform adequately in the worst case among the considered scenarios, thereby guarding against solutions that are over-tuned to a single operating point. The robustness analyses in Section 4.4 support this choice: the optimized controller preserved closed-loop stability under $\pm 10\%$ independent variation of T and R, with an ITAE deviation below 35.1%, and tolerated measurement noise of up to 10% with negligible transient degradation. Comparable robustness has been reported for GWO-optimized controllers elsewhere (for instance, robust behaviour under disturbances and parameter uncertainty in feedback-linearization designs [31,32], and in adaptive fast terminal sliding-mode control of a robotic manipulator [34]) which reinforces the suitability of GWO-based design for systems subject to uncertainty.

The choice of GWO is further supported by its convergence behaviour. All three optimizers (GWO, PSO, and GA) reached essentially the same solution across the 30 independent runs (GWO standard deviation 0.218), and the best solution ($p^* = [3.0016; 3.0015; 3.0519]$) lies in the interior of the search space, not on any bound, indicating that it is determined by the damping and stability-margin constraints rather than by the box limits. Such reproducibility and rapid convergence are precisely the properties for which GWO is favoured over PSO and GA in the comparative literature, where GWO has been reported to reach optimal controller parameters in fewer iterations and to cope better with noisy landscapes than PSO [25,26,42], although, by the No-Free-Lunch principle, no single algorithm is universally superior [27]. The consistency observed here also echoes work in the chaos domain, where metaheuristics including GWO have been employed reliably for parameter estimation and for optimizing chaotic invariants such as the Kaplan–Yorke dimension [3,36].

Several limitations should be acknowledged. First, the design rests on Jacobian linearization about the origin and therefore guarantees stabilization only within a local basin of attraction; global results would require a genuinely nonlinear controller. Second, the controller assumes full-state measurement, so a state observer would be required in a practical implementation, a need frequently addressed in the literature through observer-based, optimization-driven designs [17,21]. Third, the robustness study was restricted to independent $\pm 10\%$ parametric variations and proportional measurement noise; correlated or larger uncertainties, actuator dynamics, and transport delays were not considered. Addressing these aspects, together with chaotic-map-enhanced GWO variants that further improve search diversity [37,38], constitutes worthwhile directions for future work.

6. CONCLUSION

This study proposed an optimization-based state-feedback control framework for the local stabilization of the Moore–Spiegel chaotic oscillator. Before the control design stage, the chaotic

CC: BY-NC-ND

character of the system at ($T = 36$) and ($R = 100$) was established through a comprehensive dynamical analysis including equilibrium and local stability analysis, phase-space divergence, the Lyapunov spectrum, the Kaplan–Yorke dimension, and bifurcation behavior. On this basis, the Grey Wolf Optimizer (GWO) was employed to determine the closed-loop pole locations systematically by minimizing a composite performance index under a multi-scenario robustness formulation.

The results demonstrated that the proposed GWO-based pole-optimization strategy converged reliably to the same solution over 30 independent runs, indicating strong reproducibility of the optimization process. The resulting controller produced the optimized feedback gain vector $\left(K_{opt} = [18.9901, ; 100.3393, ; 8.0550]\right)$ and yielded a well-damped, interior closed-loop pole configuration characterized by ($\sigma = 3.0016$) and ($\zeta = 0.707$). In comparison with the conventional pole-placement baseline, the optimized controller provided substantial improvements in transient and energetic performance, reducing ISE by 83.9%, IAE by 16.5%, overshoot by 79.6%, and control energy by 94.8%. The settling time and the ITAE, by contrast, were both about four times larger than for the baseline design (a factor of roughly 4.0 and 4.1, respectively); this behavior reflects the deliberate trade-off of the low-energy, well-damped design, whose gradual, monotonic and ringing-free approach to the equilibrium enters the (2%) band later than the aggressive, oscillatory baseline response, and is accompanied by a far smaller transient excursion and control effort.

The robustness analyses further confirmed the effectiveness of the proposed design. Closed-loop stability was preserved in all nine perturbation cases generated by independent ($\pm 10\%$) variations of the nominal parameters (T) and (R), while the maximum deviation in ITAE remained below 35.1%. In addition, the controller maintained stable operation in the presence of measurement noise up to 10%, with only negligible deterioration in transient performance for noise levels up to 5%. These results indicate that the proposed method offers not only improved nominal performance but also satisfactory robustness against moderate uncertainty and noisy measurements. Overall, the findings show that GWO-based pole optimization constitutes an effective, reproducible, and energy-efficient approach for the local stabilization of chaotic nonlinear systems. The study also highlights the practical value of combining dynamical-system analysis with optimization-based controller synthesis in order to obtain controllers that are both performance-oriented and robust.

Future work may extend the present framework in several directions. First, the proposed methodology can be generalized to other chaotic oscillators and higher-dimensional nonlinear systems in order to assess its broader applicability. Second, alternative metaheuristic algorithms and hybrid optimization schemes may be investigated to compare convergence properties, solution quality, and computational efficiency. Third, the current local stabilization framework may be expanded toward more challenging control objectives such as trajectory tracking, synchronization, observer-based control, or output-feedback design. Finally, future studies may consider larger uncertainty bounds, external disturbances, actuator constraints, and real-time or hardware-based implementations to further evaluate the practical feasibility of the proposed control strategy.

Peer-review: External, Independent.

Acknowledgements:

-

Declarations:

1. Statement of Originality:

This work is original.

2. Author Contributions:

Concept: MSS,YHEN,MSD; ***Conceptualization:*** MSS,YHEN,MSD; ***Literature Search:*** MSS,YHEN,MSD; ***Data Collection:*** MSS,YHEN,MSD; ***Data Processing:*** MSS,YHEN,MSD; ***Analysis:*** MSS,YHEN,MSD; ***Writing – original draft:*** MSS,YHEN,MSD; ***Writing – review & editing:*** MSS,YHEN,MSD.

3. Ethics approval:

CC: BY-NC-ND

Not applicable.

4. Funding/Support:

This work has not received any funding or support.

5. Competing Interests:

The authors declare no competing interests.

6. GenAI Usage Statement:

No GenAI tools were used at any stage of the study.

7. Sustainable Development Goals:

REFERENCES

[1] Chang, S. C. (2020). Controlling Chaos through Period-Doubling Bifurcations in Attitude Dynamics for Power Systems. Mathematical Problems in Engineering, 2020(1), 8853459.

[2] Johansyah, M. D., Sambas, A., Zheng, S., Benkouider, K., Vaidyanathan, S., Mohamed, M. A., & Mamat, M. (2023). A novel financial system with one stable and two unstable equilibrium points: Dynamics, coexisting attractors, complexity analysis and synchronization using integral sliding mode control. Chaos, Solitons & Fractals, 177, 114283.

[3] Zainel, Q. M., Darwish, S. M., & Khorsheed, M. B. (2022). Employing quantum fruit fly optimization algorithm for solving three-dimensional chaotic equations. Mathematics, 10(21), 4147.

[4] Moore, D. W., & Spiegel, E. A. (1966). A thermally excited non-linear oscillator. Astrophysical Journal, vol. 143, p. 871, 143, 871.

[5] Bulut, G. G., Catalbas, M. C., & Güler, H. (2020). Chaotic Systems Based Real-Time Implementation of Visual Cryptography Using LabVIEW. Traitement du Signal, 37(4), 639-645.

[6] Løkse, S., Bianchi, F. M., & Jenssen, R. (2017). Training echo state networks with regularization through dimensionality reduction. Cognitive Computation, 9(3), 364-378.

[7] Ramar, R., Vaidyanathan, S., Akgul, A., & Emin, B. (2024). A new chaotic jerk system with cubic and hyperbolic sine nonlinearities and its application to random number generation and biomedical image encryption. Scientia Iranica.

[8] Li, P., Xia, L., Qian, J., & Fan, Y. (2023). Adaptive synchronization analysis of chaotic system based on memristor.

[9] Danca, M. F. (2017). Hidden chaotic attractors in fractional-order systems. Nonlinear Dynamics, 89(1), 577-586.

[10] Molla, T., Duraisamy, P., Rajagopal, K., Karthikeyan, A., & Boulaaras, S. (2024). Exploring nonlinearity in quarter car models with an experimental approach to formulating fractional order form and its dynamic analysis. Scientific Reports, 14(1), 12074.

CC: BY-NC-ND

[11] Rajagopal, K., Nazarimehr, F., Karthikeyan, A., Srinivasan, A., & Jafari, S. (2018). Fractional order synchronous reluctance motor: analysis, chaos control and FPGA implementation. Asian Journal of Control, 20(5), 1979-1993.

[12] Köse, E., & Mühürcü, A. (2018). Comparative controlling of the Lorenz chaotic system using the SMC and APP methods. Mathematical Problems in Engineering, 2018(1), 9612749.

[13] Liu, D., & Yan, G. (2020). Stabilization of chaotic systems via act-and-wait delayed feedback control using a high-precision direct integration method. SN Applied Sciences, 2(4), 521.

[14] Mutakabbir Khan, M., & Jasim Uddin, M. (2025). Complexity analysis with chaos control: A discretized ratio-dependent Holling-Tanner predator-prey model with Fear effect in prey population. PLoS One, 20(6), e0324299.

[15] Din, Q., Elsadany, A. A., & Khalil, H. (2017). Neimark-Sacker Bifurcation and Chaos Control in a Fractional-Order Plant-Herbivore Model. Discrete Dynamics in Nature and Society, 2017(1), 6312964.

[16] Vinoth, S., Sivasamy, R., Sathiyanathan, K., Unyong, B., Vadivel, R., & Gunasekaran, N. (2022). A Novel Discrete-Time Leslie–Gower Model with the Impact of Allee Effect in Predator Population. Complexity, 2022(1), 6931354.

[17] Bianchin, G., Vaquero, M., Cortés, J., & Dall'Anese, E. (2021, December). Data-driven synthesis of optimization-based controllers for regulation of unknown linear systems. In 2021 60th IEEE Conference on Decision and Control (CDC) (pp. 5783-5788). IEEE.

[18] Bekhiti, B., Dahimene, A., Nail, B., & Kamel, H. (2016). 2-Dof Block Pole Placement Control Application To: Have-Dash-IIBTT Missile. International Journal of Information Technology, Modeling and Computing (IJITMC) Vol, 4.

[19] Sababha, M., Zohdy, M., & Kafafy, M. (2019). Robust pole placement using firefly algorithm. International Journal of Electrical & Computer Engineering (2088-8708), 9(2).

[20] Gałecki, A., Michalczuk, M., Kaszewski, A., Ufnalski, B., & Grzesiak, L. M. (2020). Grid-tied converter operated under unbalanced and distorted grid voltage conditions. Bulletin of the Polish Academy of Sciences. Technical Sciences, 68(2).

[21] Abdelrahim, M., & Almakhles, D. (2023). Observer-Based Control of Inductive Wireless Power Transfer System Using Genetic Algorithm. Processes, 11(6), 1859.

[22] Mirjalili, S., Mirjalili, S. M., & Lewis, A. (2014). Grey wolf optimizer. Advances in engineering software, 69, 46-61.

[23] Reddy, A. K. V. K., & Narayana, K. V. L. (2022). Symbiotic learning grey wolf optimizer for engineering and power flow optimization problems. IEEE Access, 10, 95229-95280.

[24] Xu, Z., Yang, H., Li, J., Zhang, X., Lu, B., & Gao, S. (2021). Comparative study on single and multiple chaotic maps incorporated grey wolf optimization algorithms. IEEE Access, 9, 77416-77437.

[25] Agarwal, A., Chandra, A., Shalivahan, S., & Singh, R. K. (2018). Grey wolf optimizer: a new strategy to invert geophysical data sets. Geophysical Prospecting, 66(6), 1215-1226.

[26] Nadweh, S., Khaddam, O., Hayek, G., Atieh, B., & Alhelou, H. H. (2020). Steady state analysis of modern industrial variable speed drive systems using controllers adjusted via grey wolf algorithm & particle swarm optimization. Heliyon, 6(11).

[27] Kasap, P., & Faouri, A. O. (2024). Comparison of the meta-heuristic algorithms for maximum likelihood estimation of the exponentially modified logistic distribution. Symmetry, 16(3), 259.

[28] Sun, X., Wu, M., Yang, Z., Lei, G., & Guo, Y. (2020). High-performance control for a permanent-

CC: BY-NC-ND

magnet linear synchronous generator using state feedback control scheme plus grey wolf optimisation. IET Electric Power Applications, 14(5), 771-780.

[29] Ata, B., & Gencal, M. C. (2024). Comparison of optimization approaches on linear quadratic regulator design for trajectory tracking of a quadrotor. Evolutionary Intelligence, 17(5), 3225-3240.

[30] Sharma, R., & Kumar, V. (2025). An Enhanced LQR Control Approach for Optimal Quadrotor Regulation.

[31] Vesović, M., Jovanović, R., & Trišović, N. (2022). Control of a DC motor using feedback linearization and gray wolf optimization algorithm. Advances in Mechanical Engineering, 14(3), 16878132221085324.

[32] Dai, Y., Wang, D., & Shen, F. (2023). A robust optimal control by grey wolf optimizer for underwater vehicle-manipulator system. Plos one, 18(11), e0287405.

[33] Oliveira, J., Oliveira, P. M., Boaventura-Cunha, J., & Pinho, T. (2020). Evaluation of hunting-based optimizers for a quadrotor sliding mode flight controller. Robotics, 9(2), 22.

[34] Rezoug, A., Iqbal, J., & Tadjine, M. (2022). Extended grey wolf optimization–based adaptive fast nonsingular terminal sliding mode control of a robotic manipulator. Proceedings of the Institution of Mechanical Engineers, Part I: Journal of Systems and Control Engineering, 236(9), 1738-1754.

[35] Aghaei, V. T., SeyyedAbbasi, A., Rasheed, J., & Abu-Mahfouz, A. M. (2023). Sand cat swarm optimization-based feedback controller design for nonlinear systems. Heliyon, 9(3).

[36] Fernanda Moreno-López, M., Joel Lara-Martinez, A., Maritza Gonzalez-Zapata, A., Silva-Juarez, A., Gerardo de la Fraga, L., & Tlelo-Cuautle, E. (2025). FPGA implementation of PRNGs based on chaotic systems optimized by DE, GWO, and PSO. International Journal of Circuit Theory and Applications, 53(10), 5875-5892.

[37] Mehrotra, H., & Pal, S. K. (2018). Using chaos in grey wolf optimizer and application to prime factorization. In Soft Computing for Problem Solving: SocProS 2017, Volume 1 (pp. 25-43). Singapore: Springer Singapore.

[38] Emary, E., & Zawbaa, H. M. (2016). Impact of chaos functions on modern swarm optimizers. PloS one, 11(7), e0158738.

[39] Bajcinca, N., & Flockerzi, D. (2015). Geometric approaches to state feedback control for continuous and switched linear systems. Asian Journal of Control, 17(6), 2055-2071.

[40] Demirsoy, M. S., Sarıkaya, M. S., Kurnaz, S., El Naser, Y. H., Hazar, M. A., Coşkun, S., ... & Hazar, G. (2025). Enhancing stirring performance through chaotic position control in a magnetic stirrer. Journal of the Brazilian Society of Mechanical Sciences and Engineering, 47(11), 580.

[41] El Naser, Y. H., Demirsoy, B., Erin, K., & Demirsoy, M. S. (2025). Chaotic Speed Control of a DC Motor Using the Sprott-A System for Robotic End-Effector Applications. Black Sea Journal of Engineering and Science, 8(5), 1406-1414.

[42] Sarıkaya, M. S., Demirel, O., Kaçar, S., & Derdiyok, A. (2025). Kaotik Tabanlı Geliştirilen PSO Algoritması ile PID Kontrol Parametrelerinin Optimizasyonu ve Sistem Performansının İncelenmesi. Journal of Smart Systems Research, 6(1), 45-61.

CC: BY-NC-ND